PERGAMON

Electrochimica Acta 46 (2001) 4185–4196

ELECTROCHIMICA Acta

www.elsevier.com/locate/electacta

Modeling of the charge–discharge dynamics of lithium manganese oxide electrodes for lithium-ion batteries

E. Deiss *, D. Häringer, P. Novák, O. Haas

Paul Scherrer Institute, CH-5232 Villigen, Switzerland

Received 18 December 2000; received in revised form 7 February 2001

Abstract

The lithium insertion and extraction dynamics of spinel $LiMn_2O_4$/carbon composite electrodes used in lithium-ion batteries have been investigated. A numerical model has been developed which rationalizes these electrodes as a bed of spherical $Li_{1-\delta}Mn_2O_4$ particles ($0 \leq \delta \leq 1$, depending on the degree of insertion) with carbon as an electrically conducting additive, and with electrolyte filling the pores. It can be concluded from the simulations of potential step (PS) experiments that solid-state diffusion of lithium ions in the $Li_{1-\delta}Mn_2O_4$ particles and the electrochemical reaction at the $Li_{1-\delta}Mn_2O_4$ particle surfaces are simultaneously rate-determining. Their relative importance depends on the applied overpotential. Further, the diameter of the primary particles rather than that of the primary particle agglomerates was found to be relevant for the dynamics. From the simulations, we could evaluate a value of 2.8×10^{-13} cm^2/s for the solid-state diffusion coefficient of lithium in $Li_{1-\delta}Mn_2O_4$ particles, a value of 5.5×10^{-8} cm/s for the standard heterogeneous rate constant, and a value of 0.30 for the transfer coefficient α.

Keywords: Lithium batteries; Porous electrodes; Lithium manganese oxide; Modeling; Dynamics; Kinetics; Diffusion

1. Introduction

The high energy and power density available from lithium-ion batteries is attractive for their uses both in current high-end consumer electronics applications and for future applications as power sources for electric vehicles. In such batteries, both the negative and positive electrodes are made from electrically conductive, electrolyte-filled porous composites containing electroactive materials able to insert variable quantities of lithium. During cell discharge, lithium ions are transferred from the negative electrode through the electrolyte to the positive electrode; during charge, they are transferred in the opposite direction.

So far, the electroactive insertion materials used in commercial lithium-ion cells are based on carbon (LiC_6) and on lithium metal oxides such as $LiCoO_2$ [1]. The oxides used have several drawbacks — they are expensive, their kinetics of lithium insertion/extraction is slow for high-power applications, and $LiCoO_2$ (like $LiNiO_2$) is carcinogenic [2]. A large number of alternatives have been suggested. For economical and ecological reasons, manganese-based compounds with spinel or α-$NaFeO_2$-type structures have been investigated over the last few years. Only one of these, the spinel-type oxide $LiMn_2O_4$, has so far become commercially available in amounts in the order of 100 tons/year [3]. Thus, for battery manufacturers, $LiMn_2O_4$ is today's only alternative to $Li(Co,Ni)O_2$.

The dynamics of lithium insertion into the metal oxide in the positive electrode as well as the dynamics of lithium extraction from the negative electrode are

* Corresponding author.
E-mail address: erich.deiss@psi.ch (E. Deiss).

0013-4686/01/$ - see front matter
PII: S0013-4686(01)00703-4

limiting factors for the specific power of lithium-ion batteries during discharge. A detailed knowledge of each process affecting electrode performance is necessary for an understanding of the dynamic behavior, and would undoubtedly facilitate further electrode optimization. The most important processes influencing the electrode dynamics are the diffusion of lithium ions in solid electroactive materials such as $LiMn_2O_4$ or LiC_6, the diffusion of lithium ions in the electrolyte, and the electrochemical reaction at the active material/electrolyte interface. Additionally, factors such as the composition of the active materials, the ohmic resistances in solids, and the porosity of the electrode are important parameters to be controlled in the production of electrodes able to satisfy different application requirements.

Early modeling work on porous lithium insertion electrodes has been concerned with TiS_2 [4,5]. An infinitely high electrochemical reaction rate was assumed in these two papers and in later similar work on insertion electrodes [6]. On the other hand, it was concluded when modeling the behavior of a Li/TiS_2 cell that finite electrode kinetics must be taken into account in order to reproduce the shape of experimental discharge curves [7]. Thus, electrochemical kinetics was included when modeling the behavior of cells such as Li/solid polymer/Li_nTiS_2 [8], Li_mC_6/organic liquid/$Li_nMn_2O_4$ [9], Li/solid polymer/$Li_nMn_2O_4$ [10], Li_mC_6/organic liquid/Li_nCoO_2 (SONY cell) [10], Li_mC_6/organic liquid/$Li_nMn_2O_4$ [11], Li/solid polymer/$Li_nMn_2O_4$ [12], Li_mC_6/plasticized polymer/$Li_nMn_2O_4$ [13], Li/solid polymer/$Li_nMn_2O_4$ [14], and Li/organic liquid/$Li_nMn_2O_4$ [15]. In the absence of experimental values for the electrochemical kinetic parameters, however, highly reversible charge transfer processes were assumed in all these papers, except for Ref. [15] where finite kinetic parameters could be extracted from experiments.

In the present work, we focus our attention on diffusion and electrochemical kinetics in porous $LiMn_2O_4$/carbon composite electrodes. We present experimental data obtained with a potential step (PS) technique for the dynamic behavior of electrodes made from spinel-type $LiMn_2O_4$ with three different sizes of primary particle agglomerates having agglomerate diameters of 30, 16, and 3 μm. In these PS experiments, the applied potential of an electrode is stepped immediately at initial time. We also present a detailed numerical model for a porous $LiMn_2O_4$/carbon composite electrode which includes all the main processes and properties, and with this model we perform an analysis of the PS experiments by simulation of the experimental charge per unit electrode volume versus time curves for insertion and extraction, thus arriving at values for solid-state diffusion and electrochemical kinetic parameters.

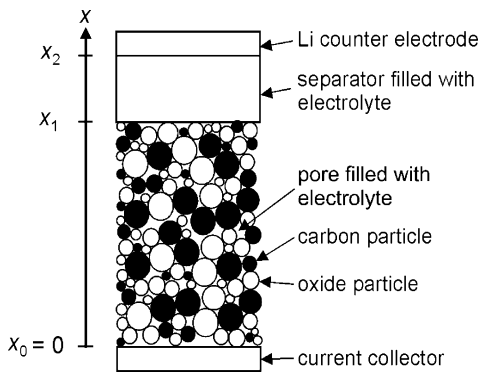

Fig. 1. Schematic drawing of a cell with $LiMn_2O_4$ and Li electrodes.

2. Experimental

2.1. Electrode preparation

Three types of $LiMn_2O_4$ electrodes have been prepared from active material in the form of three wind-separated $LiMn_2O_4$ powders, all from the same synthesis batch (Honeywell, formerly AlliedSignal/Riedel-de Haën) constituting a coarse, a medium, and a fine size-fraction of primary particle agglomerates with weight-average agglomerate diameters of 30, 16, and 3 μm, respectively. The electrode mass was an intimate mixture of 73.5 wt% $LiMn_2O_4$, 18.4 wt% carbon black (Vulcan XC 72), 6.1 wt% graphite (SFG 6, TIMCAL), and contained 2.0 wt% polyvinylidene fluoride (PVDF, Aldrich) as the binder. About 40 mg of this mixture was pressed into titanium current collectors to produce working electrodes with geometric surface areas of 1.327 cm^2, which had thicknesses of 180 μm (coarse-fraction $LiMn_2O_4$ electrode), 209 μm (medium-fraction $LiMn_2O_4$ electrode), and 265 μm (fine-fraction $LiMn_2O_4$ electrode).

2.2. Electrochemical cell

Spring-loaded two-electrode cells as described elsewhere [16], were fabricated with a metallic lithium counter electrode (Aldrich, 99.9%, 0.75 mm thickness) containing excess lithium. Prior to the experiment, the working electrode was vacuum-dried for 12 h at 120 °C [17]. Hermetically sealed cells were then assembled in an argon-filled glove box. Two layers of compressed glass fleece were used to separate the electrodes giving a total separator thickness of 0.04 cm and a separator fractional porosity of 0.6. The electrolyte was a 1 M $LiPF_6$ solution in a mixture of ethylene carbonate/dimethyl carbonate (1:1) (battery electrolyte LP30, Merck Selectipur®). A schematic drawing of such a cell is shown in Fig. 1.

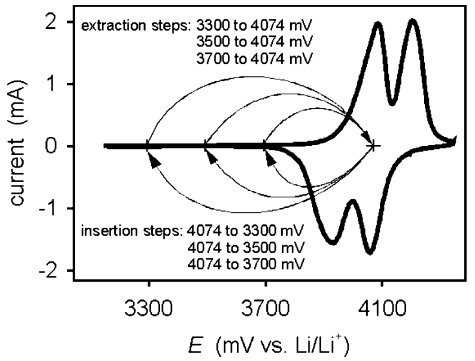

Fig. 2. Cyclic voltammogram (scan rate 33 μV/s) of a coarse-fraction $LiMn_2O_4$ electrode vs. Li/Li^+. The arrows indicate the potential steps applied in our experiments.

2.3. Cyclic voltammogram (CV)

The CV of a coarse-fraction $LiMn_2O_4$ electrode shown in Fig. 2 was recorded with a modified Wenking PGS 81 potentiostat at a scan rate of 33 μV/s.

2.4. Potential step experiments

The PS data constituting the cell's dynamic response were recorded with the same modified Wenking PGS 81 potentiostat having nine different current ranges between 1 A and 100 μA. The potentiostat was controlled by a 486-PC with software developed at the Paul Scherrer Institute. For the data exchange between the PC and the potentiostat, a 12 bit D/A and 16 bit A/D device were used as the output and input, respectively. The software included commands to trigger the potential steps of the potentiostat, change the current range, and collect the data.

The data were sampled continuously for approximately 12 h in each PS experiment. At the beginning, the sampling rate was about 1000 data points per second. As the rate of the current change decreased during a PS experiment, the data-sampling rate was reduced accordingly, and toward the end it was one data point every 250 s. Before starting a new PS experiment, we allowed 12 h for re-establishment of electrochemical equilibrium. Prior to the first PS experiment on a given electrode, the initial cell potential was maintained until the current was less than 0.15 μA/mg_{oxide}.

We restricted our PS measurements to the current waves at lower potentials in the CV shown in Fig. 2. The arrows in this figure indicate the steps performed: for lithium insertion the potential was stepped from 4074 to 3300, 3500, or 3700 mV versus Li/Li^+, for extraction it was stepped from 3300, 3500, and 3700 to 4074 mV, respectively (the step from 3700 to 4074 mV was not measured for the fine-fraction electrode). The dotted lines in Fig. 3a–c show the experimental values of charge per unit electrode volume as functions of time. This charge per unit electrode volume is uniformly distributed within the electrode only in the equilibrium state. All experiments were performed at 25 °C.

2.5. Electron microscopy

From each of the three size-fractions of $LiMn_2O_4$ (Fig. 4a–c) and from a section through a coarse-fraction agglomerate (Fig. 4d), a scanning electron microscope (SEM) image was taken using a Topcon ABT-60 instrument. Fig. 4d shows the primary particles with an

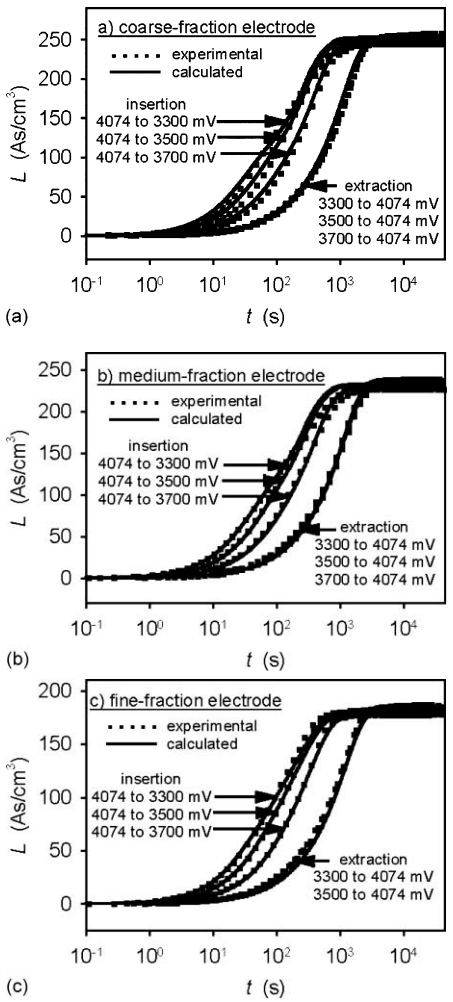

Fig. 3. Experimental and calculated charge per unit electrode volume vs. time curves for $LiMn_2O_4$/carbon composite electrodes: (a) coarse-fraction $LiMn_2O_4$ electrode (agglomerate diameter = 30 μm); (b) medium-fraction $LiMn_2O_4$ electrode (agglomerate diameter = 16 μm); and (c) fine-fraction $LiMn_2O_4$ electrode (agglomerate diameter = 3 μm).

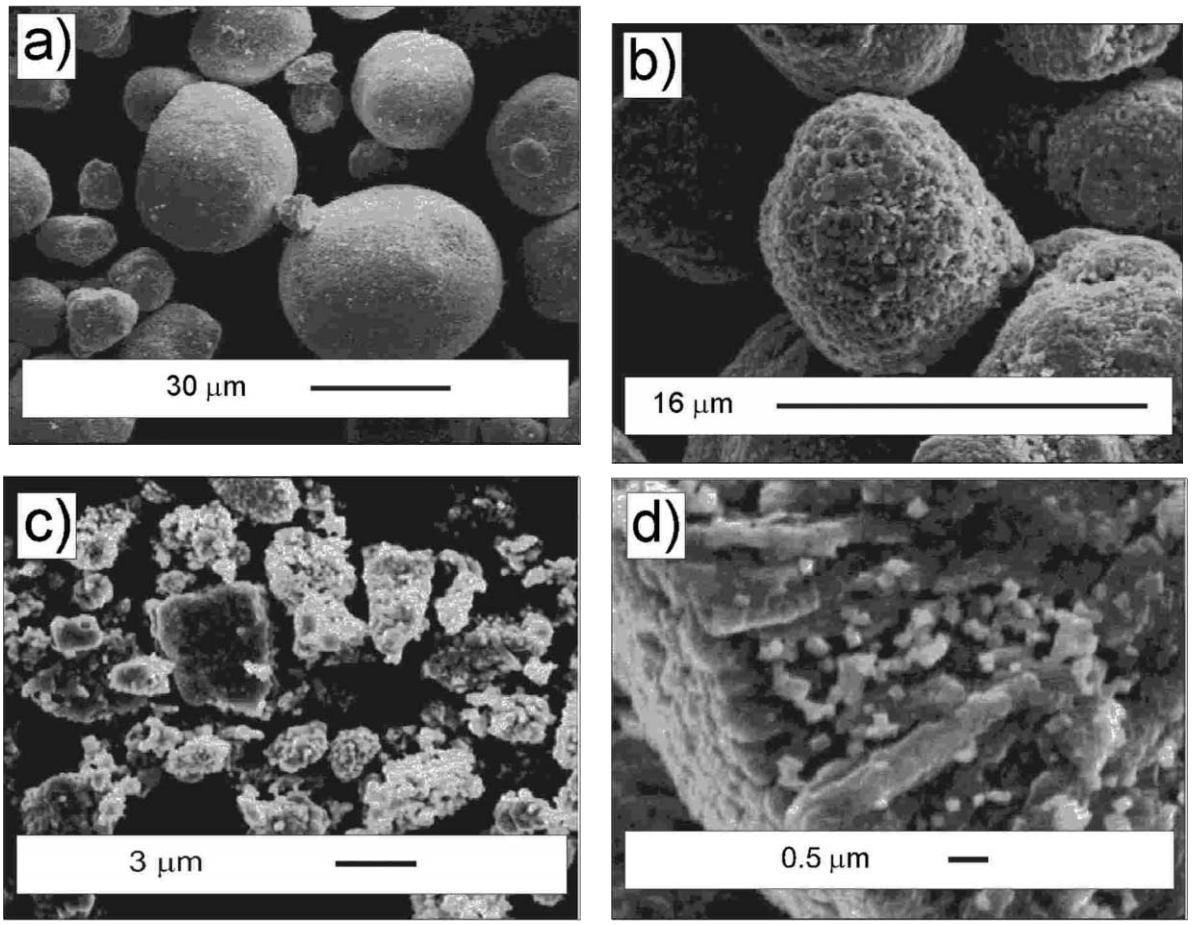

Fig. 4. SEM micrograph of: (a) the coarse-fraction $LiMn_2O_4$ (agglomerate diameter 30 μm); (b) the medium-fraction $LiMn_2O_4$ (agglomerate diameter 16 μm); (c) the fine-fraction $LiMn_2O_4$ (agglomerate diameter 3 μm); (d) a section through a coarse-fraction $LiMn_2O_4$ agglomerate showing the primary particles with an average diameter of about 0.5 μm.

average diameter of about 0.5 μm from which the agglomerates are built up.

3. Model description

In this section, we describe the physical background of our model and the corresponding set of equations used to calculate the charge per unit electrode volume versus time response in a PS experiment performed with a $LiMn_2O_4$ electrode such as that used as the positive electrode in a lithium-ion battery.

In the development of the model we only consider one single electrochemical reaction, namely, that related to the current wave at lower potentials in the CV of Fig. 2. The influence of the current wave at higher potentials in Fig. 2 and of other waves not shown in this CV (e.g. contributions of the 3-volt plateau) will be neglected.

Fig. 1 shows a schematic drawing of a $LiMn_2O_4$ electrode containing a mixture of $Li_{1-\delta}Mn_2O_4$ particles (electrochemically active material) and carbon (electrically conducting additive) pressed together with a binder and soaked in an organic electrolyte. During insertion, Li^+ ions diffuse through the electrolyte to the surface of the $Li_{1-\delta}Mn_2O_4$ particles. The penetration of Li^+ ions into the $Li_{1-\delta}Mn_2O_4$ particles is accompanied by a reduction of Mn(IV) to Mn(III) in the neighborhood of the Li^+ ions. Once penetrated, the lithium ion diffuses within the $Li_{1-\delta}Mn_2O_4$ particles while pulling along with it a nearby electron that jumps from Mn to Mn. The degree of insertion, δ, varies locally during insertion/extraction. Between the current collector and the $Li_{1-\delta}Mn_2O_4$ particles, the electrons are mainly transported via the well-conducting carbon. Our model of such an electrode accounts for the following effects:

1. diffusion of lithium ions in the $Li_{1-\delta}Mn_2O_4$ particles, which are assumed to be spherical

2. diffusion and migration of lithium ions in the electrolyte, filling the pores of the electrode and the separator
3. electrochemical reaction at the surface of the $Li_{1-\delta}Mn_2O_4$ particles
4. electrode porosity
5. ohmic resistance in the electrically conducting solid ($Li_{1-\delta}Mn_2O_4$/carbon)
6. resistance of the current collector/electrode material interface

The solution of the system of differential equations given below can be used to calculate the measured charge per unit electrode volume response of a PS experiment, including the Li^+ concentration and electric potential profile in the electrolyte, and also including the Li^+ concentration profile in the $Li_{1-\delta}Mn_2O_4$ particles.

3.1. Li^+ concentration and potential profile in the electrolyte

The Li^+ and PF_6^- diffusion and migration in the electrolyte at $x_0 < x < x_2$ (see Fig. 1), i.e. in the electrolyte between the solid electrode material and in the electrolyte of the porous separator, are governed by the flux density laws

$$N_{Li^+}^{liquid}(x,t) = -D_{Li^+}^{liquid}\cdot p(x)^{(1+\tau)}\cdot\frac{dc_{Li^+}^{liquid}(x,t)}{dx} - z_{Li^+}\cdot D_{Li^+}^{liquid} \times p(x)^{(1+\tau)}\cdot\frac{F}{RT}\cdot c_{Li^+}^{liquid}(x,t)\cdot\frac{d\varphi^{liquid}(x,t)}{dx} \quad (1)$$

$$N_{PF_6^-}^{liquid}(x,t) = -D_{PF_6^-}^{liquid}\cdot p(x)^{(1+\tau)}\cdot\frac{dc_{PF_6^-}^{liquid}(x,t)}{dx} - z_{PF_6^-}\cdot D_{PF_6^-}^{liquid} \times p(x)^{(1+\tau)}\cdot\frac{F}{RT}\cdot c_{PF_6^-}^{liquid}(x,t)\cdot\frac{d\varphi^{liquid}(x,t)}{dx} \quad (2)$$

where $N_{Li^+}^{liquid}(x,t)$ and $N_{PF_6^-}^{liquid}(x,t)$ denote the Li^+ and PF_6^- flux densities in the electrolyte, $D_{Li^+}^{liquid}$ and $D_{PF_6^-}^{liquid}$ are the diffusion coefficients of Li^+ and PF_6^- in electrolyte alone, $p(x)$ is the fractional porosity (which may be different in the electrode and separator), τ designates the tortuosity, $c_{Li^+}^{liquid}(x,t)$ and $c_{PF_6^-}^{liquid}(x,t)$ denote the concentrations of Li^+ and PF_6^- in the electrolyte, z_{Li^+} and $z_{PF_6^-}$ are the charge numbers of Li^+ and PF_6^-, t is the time, and $\varphi^{liquid}(x,t)$ is the electric potential in the electrolyte. Further, x is the coordinate position in the electrode between x_0 and x_2 (see Fig. 1), F is Faraday's constant, and F/RT is the Nernst factor. The expression for the effective diffusion coefficient in Eqs. (1) and (2), $D_i^{liquid}\cdot p(x)^{(1+\tau)}$, which accounts for the porosity and tortuosity correction, is a commonly used expression as applied, e.g. in Ref. [18]. Further, it is assumed that at any position x, the sum of the current densities in the electrically conducting solid and in the electrolyte (due to the motion of charged particles) is uniform and equal to the total current density of the cell, i.e.

$$z_{Li^+}\cdot N_{Li^+}^{liquid}(x,t)\cdot F + z_{PF_6^-}\cdot N_{PF_6^-}^{liquid}(x,t)\cdot F + i^{solid}(x,t) = i^{tot}(t) \quad (3)$$

where $i^{tot}(t)$ is the total current density of the cell (total current per geometric electrode area A), and $i^{solid}(x,t)$ is the current density in the electrically conducting solid $Li_{1-\delta}Mn_2O_4$/carbon (current per geometric electrode area A). Eq. (3) implies that the charge distribution within the cell remains constant and that, therefore, at any time t and at any position x the initial electroneutral condition is valid, i.e.

$$z_{Li^+}\cdot c_{Li^+}^{liquid}(x,t) + z_{PF_6^-}\cdot c_{PF_6^-}^{liquid}(x,t) = 0. \quad (4)$$

Eliminating $d\varphi^{liquid}(x,t)/dx$, $N_{PF_6^-}^{liquid}(x,t)$ and $c_{PF_6^-}^{liquid}(x,t)$ in Eqs. (1)–(4) and replacing z_{Li^+} and $z_{PF_6^-}$ with its values $+1$ and -1 yields

$$N_{Li^+}^{liquid}(x,t) = -\frac{2D_{Li^+}^{liquid}D_{PF_6^-}^{liquid}}{(D_{Li^+}^{liquid}+D_{PF_6^-}^{liquid})}\,p(x)^{(1+\tau)}\frac{d}{dx}c_{Li^+}^{liquid}(x,t) + \frac{D_{Li^+}^{liquid}\cdot(i^{tot}(t)-i^{solid}(x,t))}{(D_{Li^+}^{liquid}+D_{PF_6^-}^{liquid})\cdot F} \quad (5)$$

The material balance equation can then be written as

$$p(x)\cdot\frac{d}{dt}c_{Li^+}^{liquid}(x,t) = -\frac{d}{dx}N_{Li^+}^{liquid}(x,t) + q(x,t) \quad (6)$$

where $q(x,t)$ is the source density (moles per unit electrode volume and per unit time) of Li^+ due to the electrochemical reaction at the surface of the $Li_{1-\delta}Mn_2O_4$ particles, to be calculated in a separate later paragraph. At the current collector at $x = x_0$, the flux density of Li^+ vanishes, i.e.

$$N_{Li^+}^{liquid}(x_0,t) = 0 \quad (7)$$

and at the Li counter electrode side at $x = x_2$, we can write

$$N_{Li^+}^{liquid}(x_2,t) = \frac{i^{tot}(t)}{F}. \quad (8)$$

The electric potential in the solid, $\varphi_{solid}(x,t)$, relative to the potential in the lithium of the Li/Li^+ electrode is given by the applied cell potential E, diminished by the potential drop at the current collector/electrode material interface and the iR drop between x_0 and x:

$$\varphi^{solid}(x,t) = E - \sigma^{ccol}\cdot i^{tot}(t) - \int_{x_0}^{x} i^{solid}(x,t)\cdot\rho^{solid}\cdot dx \quad (9)$$

where σ^{ccol} is the resistance at the current collector/electrode material interface, and ρ^{solid} the resistivity of the solid. The potential in the electrolyte relative to the lithium in the Li/Li^+ electrode can be calculated by integrating the derivative

$$\frac{\mathrm{d}\varphi^{\mathrm{liquid}}(x,t)}{\mathrm{d}x} = \frac{1}{(D^{\mathrm{liquid}}_{\mathrm{Li}^+} + D^{\mathrm{liquid}}_{\mathrm{PF}_6^-}) \cdot p(x)^{(1+\tau)} \cdot \frac{F}{RT} \cdot c^{\mathrm{liquid}}_{\mathrm{Li}^+}(x,t)} \cdot \left(\frac{-i^{\mathrm{tot}}(t) + i^{\mathrm{solid}}(x,t)}{F} - (D^{\mathrm{liquid}}_{\mathrm{Li}^+} - D^{\mathrm{liquid}}_{\mathrm{PF}_6^-}) \cdot p(x)^{(1+\tau)} \cdot \frac{\mathrm{d}c^{\mathrm{liquid}}_{\mathrm{Li}^+}(x,t)}{\mathrm{d}x} \right) \quad (10)$$

(obtained from Eqs. (1)–(4) by eliminating $N^{\mathrm{liquid}}_{\mathrm{Li}^+}(x,t)$, $N^{\mathrm{liquid}}_{\mathrm{PF}_6^-}(x,t)$, and $c^{\mathrm{liquid}}_{\mathrm{PF}_6^-}(x,t)$ and by replacing $z_{\mathrm{Li}+}$ and $z_{\mathrm{PF}_6^-}$ with its corresponding values) and by using the Li electrode boundary condition at $x = x_2$ of

$$\varphi^{\mathrm{liquid}}(x_2,t) = E^{\mathrm{st}}_{\mathrm{Li}} - \frac{RT}{F} \cdot \ln \frac{c^{\mathrm{liquid}}_{\mathrm{Li}^+}(x_2,t)}{c^{\mathrm{st}}} \quad (11)$$

$E^{\mathrm{st}}_{\mathrm{Li}}$ is the standard potential of the Li electrode, and c^{st} is the standard concentration (mol/l) introduced to avoid a dimension in the logarithm. With Eq. (11), we implicitly assume fast kinetics for the Li electrode as compared to the $LiMn_2O_4$ electrode. This is justified since we measured at the Li electrode an overpotential of only 5 mV at a current density of 10 mA/cm^2. At the very beginning of the potential jump, the potential of the working electrode might deviate somehow from the nominal value due to high currents. However, it will not falsify the charge evolution curve significantly since only a minor part of the total charge flows under these extreme conditions.

3.2. Electrochemical reaction at the $Li_{1-\delta}Mn_2O_4$ particle surface and current density

The passage of lithium from the electrolyte into a $Li_{1-\delta}Mn_2O_4$ particle is governed by an electrochemical redox reaction at the $Li_{1-\delta}Mn_2O_4$ particle surface, which is responsible for the boundary condition of Li^+ diffusion within the $Li_{1-\delta}Mn_2O_4$ particles, for the Li^+ source density $q(x,t)$ in the electrolyte, and for the total cell current density $i^{\mathrm{tot}}(t)$. This electrochemical reaction can be formulated as

$$\mathrm{Li}^+ + \mathrm{Mn_2O_4} + \mathrm{e}^- \underset{k^{\mathrm{b}}(x,t)}{\overset{k^{\mathrm{f}}(x,t)}{\rightleftarrows}} \mathrm{LiMn_2O_4}. \quad (12)$$

This reaction occurs in two redox steps at two different potentials (see CV in Fig. 2), since two different phases are involved. In the following, we restrict our investigation to the redox step at lower potential. The kinetic expressions will be developed according to standard kinetic theory [19]. The terms $k^{\mathrm{f}}(x,t)$ and $k^{\mathrm{b}}(x,t)$ are the forward and backward heterogeneous rate constants, for which we can write the expressions

$$k^{\mathrm{f}}(x,t) = k_0 \cdot \exp\left(-\alpha \frac{F}{RT}(E_x(x,t) - E^{\mathrm{st}}_{\mathrm{LMO}}) \right) \quad (13)$$

and

$$k^{\mathrm{b}}(x,t) = k_0 \cdot \exp\left((1-\alpha) \frac{F}{RT}(E_x(x,t) - E^{\mathrm{st}}_{\mathrm{LMO}} \right) \quad (14)$$

where k_0 denotes the standard heterogeneous rate constant, α is the transfer coefficient of the electrochemical reaction, $E^{\mathrm{st}}_{\mathrm{LMO}}$ is the standard potential of the $LiMn_2O_4$ electrode, and $E_x(x,t)$ is the local difference between the potential in the $Li_{1-\delta}Mn_2O_4$ solid, $\varphi^{\mathrm{solid}}(x,t)$, and the potential in the electrolyte, $\varphi^{\mathrm{liquid}}(x,t)$, i.e.

$$E_x(x,t) = \varphi^{\mathrm{solid}}(x,t) - \varphi^{\mathrm{liquid}}(x,t) \quad (15)$$

where $\varphi^{\mathrm{solid}}(x,t)$ and $\varphi^{\mathrm{liquid}}(x,t)$ are described above. The lithium flux density $N^{\mathrm{surface}}_{\mathrm{Li}^+}(x,t)$ passing through the surface of a spherical $Li_{1-\delta}Mn_2O_4$ particle at a position x in the $LiMn_2O_4$ electrode can be expressed as follows:

$$N^{\mathrm{surface}}_{\mathrm{Li}^+}(x,t) = k^{\mathrm{f}}(x,t) \cdot c^{\mathrm{liquid}}_{\mathrm{Li}^+}(x,t) \cdot \lambda(x,t) - k^{\mathrm{b}}(x,t) \cdot c^{\mathrm{solid}}_{\mathrm{Li}^+}(x,r_1,t) \quad (16)$$

where the vacancy factor

$$\lambda(x,t) = \left(\frac{c^{\mathrm{solid}}_{\mathrm{Li}^+_{\mathrm{max}}} - c^{\mathrm{solid}}_{\mathrm{Li}^+}(x,r_1,t)}{c^{\mathrm{solid}}_{\mathrm{Li}^+_{\mathrm{max}}}} \right) \quad (17)$$

accounts for the fact that only a limited amount of Li^+, expressed as $c^{\mathrm{solid}}_{\mathrm{Li}^+_{\mathrm{max}}}$ (saturation concentration at very low potentials), can be inserted into $Li_{1-\delta}Mn_2O_4$ by the electrochemical reaction responsible for the current wave at the lower potentials in the CV of Fig. 2. The saturation concentration $c^{\mathrm{solid}}_{\mathrm{Li}^+_{\mathrm{max}}}$ used in Eq. (17) is always higher than the change in lithium concentration in the $Li_{1-\delta}Mn_2O_4$ particles during a PS experiment, because in practice the applied potentials of the PS experiment are not high or low enough to achieve complete lithium exchange of the amount of $c^{\mathrm{solid}}_{\mathrm{Li}^+_{\mathrm{max}}}$, particularly when small potential steps are applied (a complete exchange would be achieved at a hypothetical potential step from plus infinite to minus infinite volts, assuming no side reactions). The expression $c^{\mathrm{solid}}_{\mathrm{Li}^+}(x,r_1,t)$ in Eq. (17) represents the surface concentration of lithium in the $Li_{1-\delta}Mn_2O_4$ particles at position x within the $LiMn_2O_4$ electrode. Instead of our expression on the right side of Eq. (17), other authors used just the void concentration $c^{\mathrm{solid}}_{\mathrm{Li}^+_{\mathrm{max}}} - c^{\mathrm{solid}}_{\mathrm{Li}^+}(x,r_1,t)$ [20]. We prefer to divide this void concentration by $c^{\mathrm{solid}}_{\mathrm{Li}^+_{\mathrm{max}}}$ to obtain a dimensionless void factor, which ensures that $k^{\mathrm{f}}(x,t)$ and $k^{\mathrm{b}}(x,t)$ in Eq. (16) have the same dimensions as required by Eqs. (13) and (14).

The standard potential $E^{\mathrm{st}}_{\mathrm{LMO}}$ given in Eqs. (13) and (14) can be calculated from the mean value of the anodic and cathodic peak potentials of the CV given in Fig. 2. This CV is an equilibrium CV where the peak potentials E^{peak} remain constant for any further decrease of the scan rate. In such an equilibrium condition, the current of the CV is proportional to the

potential derivative of the equilibrium concentration of the active material, $dc^{solid}_{Li^+_{eq}}(E)/dE$. Therefore, the CV (i.e. the current versus E) exhibits a peak (an extreme) where $dc^{solid}_{Li^+_{eq}}(E)/dE$ versus E exhibits a peak, i.e. at that potential E where the second derivative $d^2c^{solid}_{Li^+_{eq}}(E)/dE^2$ is zero. The concentration of the active species at equilibrium condition, $c^{solid}_{Li^+_{eq}}(E)$, can be calculated from Eq. (16) (with the governing Eqs. (9)–(17) and the equilibrium conditions $c^{solid}_{Li^+}(x,r_1,t)=c^{solid}_{Li^+_{eq}}(E)$, $N^{surface}_{Li^+}(x,t)=0$, $c^{liquid}_{Li^+}(x,t)=c^{liquid}_{Li^+_{init}}$ (initial Li^+ concentration), $i^{tot}(x,t)=0$, $i^{solid}(x,t)=0$, $dc^{liquid}_{Li^+}(x,t)/dx=0$) as

$$c^{solid}_{Li^+_{eq}}(E)=\frac{c^{solid}_{Li^+_{max}}}{1+\exp\left(\frac{F}{RT}(E-E^{st}_{LMO}-E^{st}_{Li})\right)\cdot\frac{c^{solid}_{Li^+_{max}}}{c^{st}}} \tag{18}$$

and the peak potential E^{peak}, i.e. the potential where the second derivative $d^2c^{solid}_{Li^+_{eq}}(E)/dE^2$ is zero, is given by

$$E^{peak}=E^{st}_{LMO}+E^{st}_{Li}+\frac{RT}{F}\cdot\ln\left(\frac{c^{st}}{c^{solid}_{Li^+_{max}}}\right) \tag{19}$$

The standard potential E^{st}_{LMO} (vs. Li/Li^+) can now be calculated from Eq. (19), as E^{st}_{Li} (vs. Li/Li^+) is zero and $c^{solid}_{Li^+_{max}}$ is a parameter to be fitted from the experiment. In practice, the cathodic and anodic peak potentials differ by reasons given in Ref. [21] which are not considered in our model. We assume that the mean value of anodic and cathodic peak potentials is a good approximation for E^{peak} given in Eq. (19).

The local Li^+ source density $q(x,t)$ appearing in Eq. (6) can now be calculated as

$$q(x,t)=-N^{surface}_{Li^+}(x,t)\cdot S \tag{20}$$

where S designates the surface density (geometric particle surface area per unit electrode volume) of the active material. The current density in the solid material $Li_{1-\delta}Mn_2O_4$/carbon, $i^{solid}(x,t)$ (current per unit of electrode surface area A flowing towards the current collector), is then given by

$$i^{solid}(x,t)=-F\cdot\int_{x_1}^{x}q(x,t)\cdot dx. \tag{21}$$

The total current density $i^{tot}(t)$ is the current density at the current collector, i.e.

$$i^{tot}(t)=i^{solid}(x_0,t) \tag{22}$$

which allows us to calculate the charge per unit electrode volume $L(t)$ versus time curve as

$$L(t)=\frac{1}{x}\cdot\int_0^t i^{tot}(t)\,dt. \tag{23}$$

3.3. Li^+ concentration profile in $Li_{1-\delta}Mn_2O_4$ particles

The diffusion of lithium in the $Li_{1-\delta}Mn_2O_4$ particles can be expressed by Fick's second law

$$\frac{dc^{solid}_{Li^+}(x,r,t)}{dt}=D^{solid}_{Li^+}\frac{1}{r^2}\frac{d}{dr}\left(r^2\frac{dc^{solid}_{Li^+}(x,r,t)}{dr}\right) \tag{24}$$

where r designates the radial position in the spherical particle and $D^{solid}_{Li^+}$ is the diffusion coefficient of Li^+ in the $Li_{1-\delta}Mn_2O_4$ particles. In the center of the particle at $r=0$, the flux of lithium disappears for reasons of symmetry, so that

$$\frac{dc^{solid}_{Li^+}(x,r=0,t)}{dr}=0 \tag{25}$$

while at the particle surface at $r=r_1$, we can write Fick's first law

$$-D^{solid}_{Li^+}\frac{dc^{solid}_{Li^+}(x,r=r_1,t)}{dr}=N^{surface}_{Li^+}(x,t). \tag{26}$$

The lithium flux density, $N^{surface}_{Li^+}(x,t)$, caused by the electrochemical reaction is given by Eq. (16).

3.4. Initial conditions, design parameters, and material constants

To solve the partial differential equations (PDEs) (6) and (24), we need initial conditions (at time zero prior to the potential step) for the concentration of Li^+ in the electrolyte, $c^{liquid}_{Li^+}(x,t=0)$, and for the concentrations of Li^+ in the $Li_{1-\delta}Mn_2O_4$ particles, $c^{solid}_{Li^+}(r,t=0)$. The initial value of $c^{solid}_{Li^+}(r,t=0)$ in the $Li_{1-\delta}Mn_2O_4$ particles is equal to the corresponding equilibrium concentration $c^{solid}_{Li^+_{eq}}(E=E^A)$ at the cell potential prior to the potential step E^A and can be calculated using Eq. (18).

To calculate the charge per unit electrode volume versus time curve $L(t)$ Eq. (23) for a PS experiment, where the cell potential E is stepped from E^A to E^B at the beginning of the experiment, we have to know the experimental design parameters A, $c^{sep}_{Li^+}$, E^A, E^B, $p(x)$, r_1, x_1, x_2, S, and the material constants $D^{liquid}_{Li^+}$, $D^{liquid}_{PF_6^-}$, $D^{solid}_{Li^+}$, E^{peak} E^{st}_{Li}, k_0, α, ρ^{solid}, σ^{ccol}, and τ. The calculated curves $L(t)$ can then be compared with the experimental data shown in Fig. 3a–c.

4. Numerical solution

To obtain the calculated charge per unit electrode volume versus time curve $L(t)$ (Eq. (23)), we require

1. the solution for the Li^+ concentration profile in the electrolyte, $c^{liquid}_{Li^+}(x,t)$, described by the PDE (Eq. (6)),
2. the solution for the local potential difference profile in the electrolyte, $E_x(x,t)$ described by Eq. (15), and

3. the solution for the concentration profile of Li^+ in the $Li_{1-\delta}Mn_2O_4$ particles, $c^{solid}_{Li^+}(x,r,t)$, described by the PDE (Eq. (24)).

As these Eqs. (6), (15) and (24) are coupled, they must be solved simultaneously. We achieved this by an iterative solution for each time step. To solve the partial differential equations (6) and (24), the Fortran routine D03PDF from NAG (Numerical Algorithms Group) was used. This routine is based on a finite element method where the space derivatives are discretized using collocation. To avoid an undefined derivative of $p(x)$ at the $LiMn_2O_4$ electrode/separator boundary, a small interface thickness of 10^{-4} times the separator length was introduced over which a linear porosity change from the value in the $LiMn_2O_4$ electrode to that in the separator was assumed.

5. Simulation of the charge per unit electrode volume versus time curves

We simulated the experimental charge per unit electrode volume versus time curves in Fig. 3a–c using the given parameters listed in Table 1 and the fitted parameters listed in Table 2. For the radius r_1 of the $Li_{1-\delta}Mn_2O_4$ particles, we used the value applicable for the primary particles from which the agglomerates are built up. For these primary particles, an average particle diameter of 0.5 μm (i.e. a particle radius r_1 of 0.25 μm) was estimated from SEM micrographs, see, e.g. Fig. 4d. The primary particle diameter is observed to be almost identical for the three size-fractions (0.5 μm) whereas the average agglomerate diameters differ (30, 16 and 3 μm). Calculated and experimental charge per

Table 1
Given parameters used for the simulations

Geometric electrode surface area		A	1.327 cm^2 [a]
Initial Li^+ concentration		$c^{liquid}_{Li^+_{init}}$	1 mol/l [a]
Diffusion coefficient of Li^+ in electrolyte		$D^{liquid}_{Li^+}$	2.0×10^{-6} cm^2/s [b]
Diffusion coefficient of PF_6^- in electrolyte		$D^{liquid}_{PF_6^-}$	2.7×10^{-6} cm^2/s [b]
Standard potential of the Li electrode		E^{st}_{Li}	0 V vs. Li/Li^+
Peak potential in CV	(coarse-fraction electrode)	E^{peak}	4.015 V vs. Li/Li^+ [c]
	(medium-fraction electrode)	E^{peak}	4.004 V vs. Li/Li^+ [c]
	(fine-fraction electrode)	E^{peak}	4.011 V vs. Li/Li^+ [c]
Electrode thickness	(coarse-fraction electrode)	x_1	0.0180 cm [a]
	(medium-fraction electrode)	x_1	0.0209 cm [a]
	(fine-fraction electrode)	x_1	0.0265 cm [a]
Separator thickness		x_2-x_1	0.04 cm [a]
Geometric surface density	(coarse-fraction electrode)	S	0.737×10^5 cm^2/cm^3 [a]
	(medium-fraction electrode)	S	0.662×10^5 cm^2/cm^3 [a]
	(fine-fraction electrode)	S	0.518×10^5 cm^2/cm^3 [a]
Electrode porosity at $0\le x\le x_1$	(coarse-fraction electrode)	$p(x)$	0.558 [d]
	(medium-fraction electrode)	$p(x)$	0.604 [d]
	(fine-fraction electrode)	$p(x)$	0.690 [d]
Separator porosity at $x_1\le x\le x_2$		$p(x)$	0.60 [a]
Average radius of primary particles (= half diameter)		r_1	0.25 μm [e]
Resistivity of solid electrode material	($Li_{1-\delta}Mn_2O_4$/carbon)	ρ^{solid}	188 Ω cm [f]
Resistance of current collector/electrode material interface		σ^{ccol}	0.59 $\Omega\,cm^2$ [g]
Tortuosity		τ	0.5 [h]

[a] Experimental design parameters.
[b] From D_{LiPF_6} (1 M) $= 2.3\times10^{-6}$ cm^2/s and cation transport number = 0.43 [34].
[c] From CV, mean value of anodic and cathodic peak potentials.
[d] Calculated from weights, densities, and dimensions.
[e] See Fig. 4d for the 30 μm fraction; similar diameters could be observed for the other fractions.
[f] Measured in dry material [35].
[g] Measured.
[h] From Ref. [36].

Table 2
Fitted parameters

Solid-state diffusion coefficient of Li^+	$D^{solid}_{Li^+}$	2.8×10^{-13} cm^2/s
Standard heterogeneous rate constant	k_0	5.5×10^{-8} cm/s
Transfer coefficient	α	0.30
Maximum Li^+ concentration in solid (for the current wave at lower potentials in the CV shown in Fig. 2)	$c^{solid}_{Li^+_{max}}$	11.3–12.2 mol/l

unit electrode volume versus time curves are shown in Fig. 3a–c. The total of 17 experimental charge per unit electrode volume versus time curves could be fitted with identical values for $D^{solid}_{Li^+}$, k_0 and α, whereas for each experiment a separate value of $c^{solid}_{Li^+_{max}}$ was evaluated. The value of $c^{solid}_{Li^+_{max}}$ varies slightly due to capacity losses between different steps.

A fit of the experimental charge per unit electrode volume versus time curves with identical values for $D^{solid}_{Li^+}$, k_0 and α could not be achieved when using the agglomerate diameters of 30, 16 and 3 μm (i.e. a radius r_1 of 15, 8 and 1.5 μm) as particle diameter for the three size-fractions. Identical values for $D^{solid}_{Li^+}$, k_0 and α must be expected, because the three size-fractions of $LiMn_2O_4$ were all prepared in the same batch and separated mechanically.

While fitting the experimental curves we noticed that the calculated charge insertion curves in Fig. 3a–c become more sensitive to the selection of $D^{solid}_{Li^+}$ (as compared to the selection of k_0), the lower the applied potential of the PS. In a potential step to 3300 mV, the calculated charge insertion curves are almost insensitive to the selection of k_0. The corresponding charge extraction curves are sensitive to the selection of both $D^{solid}_{Li^+}$ and k_0. An increase of $c^{solid}_{Li^+_{max}}$ spreads the curves proportionally along the ordinate.

6. Discussion

6.1. Rate-determining step

An optimized fit of the set of charge per unit electrode volume versus time curves (Fig. 3a–c) can only be achieved by using both $D^{solid}_{Li^+}$ and k_0 as the fitting parameters. This means that two steps, solid-state diffusion in the $Li_{1-\delta}Mn_2O_4$ particles and the electrochemical reaction at the surface of the $Li_{1-\delta}Mn_2O_4$ particles, are simultaneously rate-determining. Their relative importance depends on the experimental conditions. With decreasing applied potential E, the calculated insertion curves become more sensitive to $D^{solid}_{Li^+}$ (and less sensitive to k_0), which implies that solid-state diffusion becomes more and more rate-determining with decreasing applied potential in the insertion process. This observation can be explained by the fact that, for Li^+ insertion, a PS with an applied potential far away from the standard potential (see Fig. 1) produces a large overpotential thus giving rise to a very fast electrochemical reaction. The lithium rapidly enters the $Li_{1-\delta}Mn_2O_4$ particles on account of this electrochemical reaction, but then cannot move on rapidly enough towards the particle center due to rate-determining solid-state diffusion. At smaller overpotentials, the electrochemical reaction tends to become more important. A rate-determining combination of lithium transfer through the particle surface and lithium diffusion within the particle had also been deduced from ac measurements at $LiNiO_2$ electrodes [22], while ac impedance measurements at TiS_2 electrodes had indicated that here, lithium transfer through the particle surface was rate-determining [23].

6.2. Insertion and extraction rates

Due to the fact that the overpotential for the insertion PS is higher than that for extraction, shorter half-charge times $T_{1/2}$ (the time at which half of the final charge per unit electrode volume is reached) are observed for insertion than for extraction (see Fig. 3a–c). The end potential for extraction is close to the standard potential in all extraction experiments (see Fig. 1), and the overpotential driving extraction is smaller than that driving insertion, which results in slower extraction rates. Our model predicts this behavior quantitatively.

Similar effects have been revealed in carbon electrodes [24,25], and interpreted qualitatively in terms of solid-state diffusion coefficients which depend on the degree of insertion [25].

6.3. Agglomerate and primary particle size-dependence of charge and discharge rates

From our simulations, it can be concluded that the observed primary particle diameter is decisive for the kinetics of the $LiMn_2O_4$ electrode, while the agglomerate diameter has almost no influence on the kinetics. This suggests that the pores within the agglomerates are completely filled with electrolyte. This finding is supported by the micrograph reproduced in Fig. 4d, which shows that the interior of an agglomerate consists of a

loose framework of primary particles. That the agglomerate diameters have no influence on the insertion or extraction rate is also obvious from Fig. 3a–c, where the experimental charge and discharge curves for a given PS hardly differ between $LiMn_2O_4$ electrodes prepared with different agglomerate size-fractions. As observed elsewhere [26] for porous $LiCoO_2$/carbon composite electrodes, different particle sizes have no effect on the rate capability, but it is not clear whether in these cases different primary particle sizes or different agglomerate sizes were involved.

6.4. Solid-state diffusion coefficients $D_{Li^+}^{solid}$ in $Li_{1-\delta}Mn_2O_4$

The experiments can be fitted with our model using a solid-state diffusion coefficient $D_{Li^+}^{solid}$ which is independent of the degree of insertion δ, and which has a value of 2.8×10^{-13} cm^2/s (Table 2). This value is lower than published diffusion coefficients obtained with other methods. Thus, a value of 10^{-9} cm^2/s was obtained with a potentiostatic intermittent titration technique (PITT) [27]. Values between 4×10^{-8} and 10^{-9} cm^2/s which varied with the degree of insertion, exhibited two distinct minima, and differed between charge and discharge, were found with an electrochemical voltage step (EVS) technique [28]. Values between 1.3×10^{-8} and 2.1×10^{-9} cm^2/s which varied with the degree of insertion and differed between charge and discharge were obtained using a galvanostatic intermittent titration technique (GITT) [28]. A value of 8.3×10^{-11} cm^2/s was obtained for extraction within the current wave at lower potentials of CV such as that in Fig. 2, one of 9.5×10^{-11} cm^2/s was obtained for extraction within the current wave at higher potentials, and values of 1.4×10^{-10} and 6.6×10^{-11} cm^2/s were obtained for the corresponding insertion processes using a PS technique [29]. A diffusion coefficient varying with the degree of insertion δ between values of 1.9×10^{-12} and 3.1×10^{-11} cm^2/s (fastest value at $\delta = 0.5$) was found using ac impedance [30]. A value of 2.5×10^{-11} cm^2/s was found using GITT [31]. A diffusion coefficient having values between 10^{-10} and 10^{-13} cm^2/s which varied with the degree of insertion and exhibited two minima was found using a PITT technique [32], and finally values in the range 9.2×10^{-10} to 2.6×10^{-8} cm^2/s were found using ac impedance [15]. We attribute most of these dissimilarities to the fact that some authors used the value of the agglomerate diameter of $Li_{1-\delta}Mn_2O_4$ rather than that of the primary particle diameter as applicable particle diameter. Different preparation methods of $Li_{1-\delta}Mn_2O_4$ or the use of different evaluation methods may also lead to different values for the diffusion coefficient $D_{Li^+}^{solid}$.

Our model can fit the experiments with a diffusion coefficient $D_{Li^+}^{solid}$ that is independent of the degree of Li^+ insertion δ, although several authors could only explain their experiments with a δ-dependent diffusion coefficient as mentioned above [15,28,30,32].

An effect of a passivating film (solid electrolyte interphase, SEI) formed at the surface of the $Li_{1-\delta}Mn_2O_4$ particles due to solvent oxidation [33] is neglected in our model. This approximation is valid insofar as lithium transport through the SEI is reported to be fast and not rate-determining [25]. We also neglected the fact that the porosity within the agglomerates is different from that between the agglomerates.

6.5. Standard heterogeneous rate constant k_0

Our value of 5.5×10^{-8} cm/s for the standard heterogeneous rate constant k_0 points to a slow electrochemical reaction rate. Similar values between 2.2×10^{-8} and 1.7×10^{-7} cm/s have been obtained from cyclic voltammograms [29].

6.6. Transfer coefficient α

The value of 0.30 obtained for the transfer coefficient α of the electrochemical reaction (Eq. (12)) can be explained by the fact that electron transfer is associated with a very asymmetric liquid/solid insertion process.

7. Conclusions

Potential step experiments have been performed on $LiMn_2O_4$ electrodes. The dynamic response was analyzed with a numerical model based on the principal physical processes occurring during charge and discharge. For the process of lithium insertion and extraction, it can be concluded that solid-state diffusion in the $Li_{1-\delta}Mn_2O_4$ particles and the electrochemical reaction at the surface of the $Li_{1-\delta}Mn_2O_4$ particles are simultaneously rate-determining. Their relative importance depends on the applied overpotential. Simulations of the data obtained in a total of 17 PS experiments with considerably different experimental conditions yielded a best-fit value of 2.8×10^{-13} cm^2/s for the diffusion coefficient $D_{Li^+}^{solid}$of lithium in the $Li_{1-\delta}Mn_2O_4$ particles, a value of 5.5×10^{-8} cm/s for the standard heterogeneous rate constant k_0, and a value of 0.30 for the transfer coefficient α. Simulations also revealed that the diameter of the $Li_{1-\delta}Mn_2O_4$ primary particles rather than their agglomerate diameter is responsible for the insertion and extraction dynamics. This suggests that the microporous $Li_{1-\delta}Mn_2O_4$ agglomerates are completely soaked with electrolyte.

8. List of symbols

A	geometric surface area of the electrode, cm^2
$c^{liquid}_{Li^+}(x,t)$	Li^+ concentration in the electrolyte (moles per unit volume of electrolyte), mol/cm^3
$c^{liquid}_{PF_6^-}(x,t)$	PF_6^- concentration in the electrolyte (moles per unit volume of electrolyte), mol/cm^3
$c^{liquid}_{Li^+_{init}}$	initial Li^+ concentration in the electrolyte (moles per unit volume of electrolyte) prior to the potential step, mol/cm^3
$c^{solid}_{Li^+}(x,r,t)$	Li^+ concentration in the $Li_{1-\delta}Mn_2O_4$ particles (moles per unit volume of solid), mol/cm^3
$c^{solid}_{Li^+_{eq}}(E)$	equilibrium concentration of Li^+ in the $Li_{1-\delta}Mn_2O_4$ particles at a given applied cell potential E, mol/cm^3
$c^{solid}_{Li^+_{max}}$	maximum concentration of Li^+ that can be inserted into $Li_{1-\delta}Mn_2O_4$ by the electrochemical reaction which is responsible for the current wave at lower potentials in the CV of Fig. 2, mol/cm^3
c^{st}	standard concentration, 1 mol/l
$D^{liquid}_{Li^+}$	diffusion coefficient of Li^+ in the electrolyte, cm^2/s
$D^{liquid}_{PF_6^-}$	diffusion coefficient of PF_6^- in the electrolyte, cm^2/s
$D^{solid}_{Li^+}$	diffusion coefficient of Li^+ in the $Li_{1-\delta}Mn_2O_4$ particles, cm^2/s
E	applied cell potential, V
E^A	cell potential prior to the potential step, V
E^B	cell potential after the potential step, V
E^{st}_{Li}	standard potential of the Li electrode, V
E^{st}_{LMO}	standard potential of the $LiMn_2O_4$ electrode reaction causing the current wave at lower potentials in the CV of Fig. 2, V
E^{peak}	peak potential in the cyclic voltammogram (mean value of anodic and cathodic peak potentials in the current wave at lower potentials in the CV of Fig. 2), V
$E_x(x,t)$	local difference between the potentials of the $Li_{1-\delta}Mn_2O_4$ solid and the electrolyte, V
F	Faraday's constant, As/mol
F/RT	Nernst factor, V^{-1}
$i^{solid}(x,t)$	current density (current per geometric electrode area A) in the electrically conducting solid ($Li_{1-\delta}Mn_2O_4$/carbon) at position x within the $LiMn_2O_4$ electrode, A/cm^2
$i^{tot}(t)$	total current density (current per geometric electrode area A) of the cell, A/cm^2
k_0	standard heterogeneous rate constant, cm/s
$k^b(x,t)$	backward heterogeneous rate constant, cm/s
$k^f(x,t)$	forward heterogeneous rate constant, cm/s
$L(t)$	charge per unit electrode volume during a PS experiment, As/cm^3
$N^{liquid}_{Li^+}(x,t)$	Li^+ flux density in the electrolyte, $mol/cm^2/s$
$N^{liquid}_{PF_6^-}(x,t)$	PF_6^- flux density in the electrolyte, $mol/cm^2/s$
$N^{surface}_{Li^+}(x,t)$	lithium flux density through the $Li_{1-\delta}Mn_2O_4$ particle surface due to the electrochemical reaction, $mol/cm^2/s$
$p(x)$	fractional porosity of the $LiMn_2O_4$ electrode
$q(x,t)$	Li^+ source density (moles per unit electrode volume per unit time) due to the electrochemical reaction, $mol/cm^3/s$
r	radial position in a spherical $Li_{1-\delta}Mn_2O_4$ particle, cm
r_1	radial position at the surface of a spherical $Li_{1-\delta}Mn_2O_4$ particle (r_1 = half diameter), cm
S	surface density of the active $Li_{1-\delta}Mn_2O_4$ particles (geometric surface area of the particles per unit electrode volume), cm^2/cm^3
t	time, s
$T_{1/2}$	half-charge time (time at which half of the total charge per unit electrode volume has been reached in Fig. 3a–c), s
x	position in x-direction within the cell (see Fig. 1), cm
x_0	x-value at the current collector/$LiMn_2O_4$ electrode interface (see Fig. 1), cm
x_1	x-value at the $LiMn_2O_4$ electrode/separator interface (see Fig. 1), cm
x_2	x-value at the Li electrode (see Fig. 1), cm
z_{Li^+}	charge number of Li^+ $(+1)$
$z_{PF_6^-}$	charge number of PF_6^- (-1)
α	transfer coefficient of the electrochemical reaction
δ	degree of insertion, stoichiometric index in $Li_{1-\delta}Mn_2O_4$
$\lambda(x,t)$	vacancy factor in the electrochemical reaction law which limits the Li^+ concentration in $Li_{1-\delta}Mn_2O_4$ due to a limited amount of positions (vacancies) available for the Li^+ ion to be inserted
$\varphi^{liquid}(x,t)$	electric potential in the electrolyte, V

$\varphi^{solid}(x,t)$	electric potential in the solid ($Li_{1-\delta}Mn_2O_4$/carbon), V
ρ^{solid}	average resistivity of the electrically conducting solids ($Li_{1-\delta}Mn_2O_4$/carbon), Ω cm
σ^{ccol}	resistance of the current collector/electrode material interface, Ω cm^2
τ	tortuosity

Acknowledgements

We thank the Swiss Federal Office of Energy, Bern, for financial support, Mr H. Krampitz (Honeywell) for the donation of oxide samples, Professor A. Wokaun (Paul Scherrer Institute) for fruitful discussions, and Dr K. Müller (Battelle) for helpful suggestions and a careful reading of the manuscript.

References

[1] T. Ohzuku, in: G. Pistoia (Ed.), Lithium Batteries. New Materials, Developments and Perspectives, Elsevier, Amsterdam, 1994, p. 239.
[2] MERCK Safety Data Sheets No. 101183 and 101185, 1997.
[3] BASF/EMTEC Magnetics Product Information Sheet, Ludwigshafen, Germany, October 1999.
[4] K. West, T. Jacobsen, S. Atlung, J. Electrochem. Soc. 129 (1982) 1480.
[5] Z. Mao, R.E. White, J. Power Sources 43–44 (1993) 181.
[6] G.S. Nagarajan, J.W. Van Zee, R.M. Spotnitz, J. Electrochem. Soc. 145 (1998) 771.
[7] R.M. Spotnitz, D. Zuckerbrod, S.L. Johnson, J.T. Lundquist, R.E. White, in: R.E. White, M.W. Verbrugge, J.F. Stockel (Eds.), Modeling of Batteries and Fuel cells. In: The Electrochemical Society Proceedings Series, vol. PV-91-10, The Electrochemical Society, Pennington, NJ, 1991, p. 92.
[8] M. Doyle, T.F. Fuller, J. Newman, J. Electrochem. Soc. 140 (1993) 1526.
[9] T.F. Fuller, M. Doyle, J. Newman, J. Electrochem. Soc. 141 (1994) 1.
[10] T.F. Fuller, M. Doyle, J. Newman, J. Electrochem. Soc. 141 (1994) 982.
[11] M. Doyle, T.F. Fuller, J. Newman, in: N. Doddapaneni, A.R. Landgrebe (Eds.), Proceedings of the Symposium on Lithium Batteries, 1994, p. 37.
[12] M. Doyle, J. Newman, J. Electrochem. Soc. 54 (1995) 46.
[13] M. Doyle, J. Newman, A.S. Gozdz, C.N. Schmutz, J.-M. Tarascon, Electochim. Acta 143 (1996) 1890.
[14] M. Doyle, J. Newman, J. Appl. Electrochem. 27 (1997) 846.
[15] D. Zhang, B.N. Popov, R.E. White, J. Electrochem. Soc. 147 (2000) 831.
[16] P. Novák, W. Scheifele, F. Joho, O. Haas, J. Electrochem. Soc. 142 (1995) 2544.
[17] D. Häringer, P. Novák, O. Haas, A. Wokaun, Electrochem. Soc. Proc. Ser. PV 98-16 (1998) 296.
[18] W.G. Sunu, D.N. Bennion, J. Electrochem. Soc. 127 (1980) 2007.
[19] A.J. Bard, L.R. Faulkner, Electrochemical Methods, Wiley, New York, 1980 (chap. 3.4).
[20] C.A.C. Sequeira, A. Hooper, Solid State Ionics 9/10 (1983) 1131.
[21] S.W. Feldberg, I. Rubinstein, J. Electroanal. Chem. 240 (1988) 1.
[22] H. Li, Z. Lu, H. Huang, X. Huang, L. Chen, Ionics 2 (1996) 259.
[23] P.G. Bruce, M.Y. Saïdi, Solid State Ionics 51 (1992) 187.
[24] Z. Zhang, Rechargeable lithium and lithium-ion batteries, in: S. Megahed, B. Barnett, L. Xie (Eds.), Electrochemical Society Proceedings, vol. 94-28, 1995, p. 165.
[25] T.D. Tran, J.H. Feikert, R.W. Pekala, K. Kinoshita, J. Appl. Electrochem. 26 (1996) 1161.
[26] S.P. Sheu, C.Y. Yao, J.M. Chen, Y.C. Chiou, J. Power Sources 68 (1997) 533.
[27] D. Guyomard, J.M. Tarascon, J. Electrochem. Soc. 139 (1992) 937.
[28] J. Barker, K. West, Y. Saïdi, R. Pynenburg, B. Zachau-Christiansen, R. Koksbang, J. Power Sources 54 (1995) 475.
[29] H. Kanoh, Q. Feng, Y. Miyai, K. Ooi, J. Electrochem. Soc. 142 (1995) 702.
[30] H. Kanoh, Q. Feng, T. Hirotsu, K. Ooi, J. Electrochem. Soc. 143 (1996) 2610.
[31] K.A. Striebel, C.Z. Deng, S.J. Wen, E.J. Cairns, J. Electrochem. Soc. 143 (1996) 1821.
[32] D. Aurbach, M.D. Levi, E. Levi, H. Teller, B. Markovsky, G. Salitra, U. Heider, L. Heider, J. Electrochem. Soc. 145 (1998) 3024.
[33] T. Eriksson, T. Gustafsson, J.O. Thomas, Lithium batteries, in: S. Surampudi, R. Marsh (Eds.), Electrochemical Society Proceedings, vol. 98-16, 1998, p. 315.
[34] C. Capiglia, Y. Saito, H. Kageyama, P. Mustarelli, T. Iwamoto, T. Tabuchi, H. Tukamoto, J. Power Sources 81-82 (1999) 859.
[35] D. Häringer, Diss. ETH Zürich Nr. 13237, 1999.
[36] R.K. Schofield, C. Dakshinamurti, Discuss. Faraday Soc. 3 (1948) 56.